

## NUMERICAL MATHEMATICS OF THE SUBTRACTION METHOD FOR THE MODELING OF A CURRENT DIPOLE IN EEG SOURCE RECONSTRUCTION USING FINITE ELEMENT HEAD MODELS\*

C. H. WOLTERS<sup>†</sup>, H. KÖSTLER<sup>‡</sup>, C. MÖLLER<sup>‡</sup>, J. HÄRDTLEIN<sup>‡</sup>, L. GRASEDYCK<sup>§</sup>,  
AND W. HACKBUSCH<sup>§</sup>

**Abstract.** In electroencephalography (EEG) source analysis, a dipole is widely used as the model of the current source. The dipole introduces a singularity on the right-hand side of the governing Poisson-type differential equation that has to be treated specifically when solving the equation toward the electric potential. In this paper, we give a proof for existence and uniqueness of the weak solution in the function space of zero-mean potential functions, using a subtraction approach. The method divides the total potential into a singularity and a correction potential. The singularity potential is due to a dipole in an infinite region of homogeneous conductivity. We then state convergence properties of the finite element (FE) method for the numerical solution to the correction potential. We validate our approach using tetrahedra and regular and geometry-conforming node-shifted hexahedra elements in an isotropic three-layer sphere model and a model with anisotropic middle compartment. Validation is carried out using sophisticated visualization techniques, correlation coefficient (CC), and magnification factor (MAG) for a comparison of the numerical results with analytical series expansion formulas at the surface and within the volume conductor. For the subtraction approach, with regard to the accuracy in the anisotropic three-layer sphere model (CC of 0.998 or better and MAG of 4.3% or better over the whole range of realistic eccentricities) and to the computational complexity, 2mm node-shifted hexahedra achieve the best results. A relative FE solver accuracy of  $10^{-4}$  is sufficient for the used algebraic multigrid preconditioned conjugate gradient approach. Finally, we visualize the computed potentials of the subtraction method in realistically shaped FE head volume conductor models with anisotropic skull compartments.

**Key words.** source reconstruction, EEG, finite element method, dipole, subtraction method, algebraic multigrid, validation in three-layer sphere models, realistic head models, conductivity, anisotropy

**AMS subject classifications.** 35J25, 35Q80, 65N12, 65N21, 65N30, 65N50, 65N55, 65Y20, 68U20, 92C50

**DOI.** 10.1137/060659053

**1. EEG source reconstruction.** Electroencephalography (EEG) based source reconstruction of cerebral activity (the EEG *inverse problem*) with respect to the individual anatomy is common practice in clinical routine and research and in cognitive neuroscience. The inverse methods are based on solutions to the corresponding

---

\*Received by the editors May 5, 2006; accepted for publication (in revised form) April 5, 2007; published electronically November 7, 2007. This work was supported by the Deutsche Forschungsgemeinschaft (WO1425/1-1, GR3179/1-1), the IST-program of the European Community, project SIMBIO (<http://www.simbio.de>), and the NIH NCRR Center for Integrative Biomedical Computing (<http://www.sci.utah.edu/cibc>).

<http://www.siam.org/journals/sisc/30-1/65905.html>

<sup>†</sup>Corresponding author. Institut für Biomagnetismus und Biosignalanalyse, Westfälische Wilhelms-Universität Münster, Malmedyweg 15, 48149 Münster, Germany; Max-Planck-Institut für Mathematik in den Naturwissenschaften, Inselstrasse 22, 04103 Leipzig, Germany; Scientific Computing and Imaging Institute, University of Utah, Salt Lake City, UT 84112 ([carsten.wolters@uni-muenster.de](mailto:carsten.wolters@uni-muenster.de)).

<sup>‡</sup>Institut für Informatik 10 (Systemsimulation), Universität Erlangen-Nürnberg, Cauerstrasse 6, D-91058 Erlangen, Germany ([harald.koestler@informatik.uni-erlangen.de](mailto:harald.koestler@informatik.uni-erlangen.de), [chris.moeller@gmx.de](mailto:chris.moeller@gmx.de), [haerdtlein@informatik.uni-erlangen.de](mailto:haerdtlein@informatik.uni-erlangen.de)).

<sup>§</sup>Max-Planck-Institut für Mathematik in den Naturwissenschaften, Inselstrasse 22, 04103 Leipzig, Germany ([lgr@mis.mpg.de](mailto:lgr@mis.mpg.de), [wh@mis.mpg.de](mailto:wh@mis.mpg.de)).

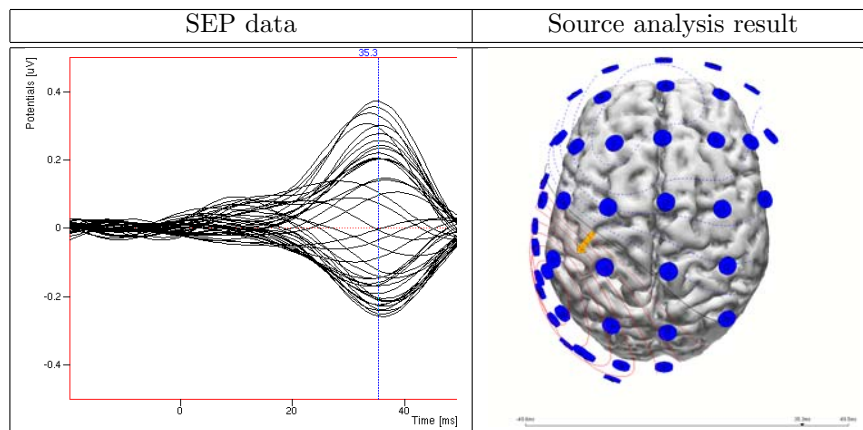


FIG. 1.1. *Left: Tactile somatosensory evoked potentials (SEP): Butterfly plot of the averaged EEG data. The peak of the SEP signal component of interest at 35.3ms is marked. Right: Reconstructed current dipole in somatosensory cortex (SI) with a remaining variance to the data of less than 1%.*

*forward problem*, i.e., the simulation of the electric potential in the head volume conductor for a *primary source*. The primary sources to be reconstructed in the inverse problem are electrolytic currents within the dendrites of the large pyramidal cells of activated neurons in the cortex sheet of the human brain. A primary source is generally formulated as an ideal or *mathematical point current dipole* [22, 24]. Such a focal brain activation can, e.g., be observed in epilepsy [29] (interictal spikes) or can be induced by a stimulus in neurophysiological or neuropsychological experiments, e.g., somatosensory or auditory evoked fields [20, 25]. Source analysis of individual somatosensory evoked potential (SEP) data is of high clinical interest for precise non-invasive localization of the central sulcus in the case of lesions lying in or adjacent to the sensorimotor region. This example from the wide application field of EEG source analysis will now be used to give a general motivation for this paper: Tactile stimuli were presented onto the right index finger tip of a 39 year old healthy male right-handed subject using balloon diaphragms driven by bursts of compressed air. Following [20], the optimal interstimulus interval of 1 sec. ( $\pm 10\%$  variation) was used and 3 runs of 600 epochs each were recorded. After band-pass filtering and artifact rejection, the remaining epochs were averaged, resulting in a signal-to-noise ratio of more than 21. A butterfly plot of the measured SEP is shown in Figure 1.1 (left). A current dipole was then reconstructed at the peak of the early component at 35.3ms using a simulated annealing (SA) optimization procedure on a presegmented triangulated surface 2mm below the cortex surface. A finite element head model with anisotropic skull compartment was used to solve the corresponding forward problems. The remaining variance of the dipole solution to the data was less than 1%. The result, shown in Figure 1.1 (right), agrees well with a recent paper showing that the early tactile somatosensory component arises from area 3b of the primary somatosensory cortex (SI) contralateral to the side of stimulation [20].

**2. Introduction.** In addition to the finite difference method (see, e.g., [15]), the finite element (FE) method [36, 2, 1, 5, 6, 18, 30, 17, 27, 21, 34] has become popular to solve the forward problem because it allows a realistic representation of the head volume conductor with its various tissue geometries and conductivities. Im-

proved mathematical algorithms, increased power of state-of-the-art computational platforms, and modern imaging methods allow today's use of the FE method for practical localization problems [30, 31, 11, 32]. In [5, 18, 34], the influence of conductivity anisotropy of the human skull, and in [17, 34], the influence of conductivity anisotropy of brain white matter were examined with regard to source reconstruction, motivating the use of three-dimensional (3D) methods when compared to spherical head models (see, e.g., [23]) or the boundary element method (see, e.g., [10]). In FE analysis, it is yet theoretically unclear how to treat *local* (in contrast to the above *remote*) anisotropy, i.e., tissue conductivity anisotropy in the direct environment of the source (cortical conductivity anisotropy). Because of its moderate anisotropy, the cortex is generally modeled as isotropic.

In the case of a point current dipole in the brain, the singularity of the potential at the source position can be treated with the so-called *subtraction method*, where the total potential is divided into the analytically known singularity potential and the singularity-free correction potential, which can then be approximated numerically using an FE approach [2, 1, 5, 18, 27]. In addition to the subtraction method, *direct approaches* to the total potential were developed, where either partial integration over the point source on the right-hand side of the weak FE formulation was used, approximating the source singularity by means of a projection in the function space of the FE trial-functions [30, 21], or the point dipole was approximated by a smoother monopolar primary source distribution [36, 6, 31, 27]. Even if it is known that the direct approaches perform reasonably well in locally isotropic spherical head model validation studies, it is impossible to formulate a satisfying FE theory if the mathematical dipole, being widely used in source reconstruction (especially also sphere and BE forward modeling) [22, 24], is used as the model for a primary source. Our study will therefore focus on the computationally more expensive (when compared to the direct approaches) FE subtraction method, where also, until now, no sufficient theory concerning existence and uniqueness of a solution and FE convergence properties was shown. Furthermore, the theory of the subtraction method was presented only for multicompartments models with an isotropic conductivity in the source environment. Either tetrahedra [2, 5, 18] or regular hexahedra [27] elements were used, but no comparison of different element types was found with regard to their numerical properties. The use of standard direct (banded LU factorization for a two-dimensional (2D) source analysis scenario [1]) or iterative (conjugate gradient (CG) without preconditioning [2] or successive overrelaxation (SOR) [27]) FE solver techniques limited the overall resolution. Therefore, local mesh refinement strategies around the source location were proposed to reduce the otherwise unacceptably large numerical errors for eccentric sources [2, 5], or specific symmetrical implementations were carried out which are useful only in a spherical volume conductor [27]. With regard to the inverse problem, local mesh refinement strategies around the source location are rather complicated to implement and time-consuming to compute and thus might not be appropriate for practical application.

In this paper, we formulate the theory of the subtraction approach for both locally isotropic and anisotropic conductivity and give a proof for existence and uniqueness of a weak solution in a zero-mean function space. We examine the FE convergence properties for the singularity-free correction potential and thus gain deep insight into the theory and practice of the method. The presented theory is valid for both EEG but also magnetoencephalography (MEG) source reconstruction. We examine the necessary accuracies of an algebraic multigrid preconditioned CG (AMG-CG) solver

for the correction potential and describe how the subtraction approach is combined with our recent work on lead field bases [32]. This combination also allows sufficiently fast solutions to the EEG and MEG inverse problems. We then consider 3D three-layer sphere model scenarios to validate our approach in isotropic models and in models with an anisotropic skull compartment. The validation of other anisotropy types would exceed the scope of this paper. We use globally high mesh resolutions for both tetrahedra and hexahedra elements which results in a sufficient accuracy for the whole range of realistic source eccentricities. We show that regular hexahedra and especially geometry-conforming node-shifted hexahedra elements perform better than tetrahedra elements. We finally apply the method to three-compartment realistically shaped volume conductor models with anisotropic skull compartments obtained from MR images of the human head.

### 3. Forward problem formulation.

**3.1. The Maxwell equations.** Let us begin with the introduction of the necessary notation: let  $\mathbf{E}$  and  $\mathbf{D}$  be the electric field and electric displacement, respectively,  $\rho$  the electric free charge density,  $\epsilon$  the electric permittivity, and  $\mathbf{j}$  the electric current density. By  $\mu$  we denote the magnetic permeability and by  $\mathbf{H}$  and  $\mathbf{B}$  the magnetic field and induction, respectively.

In the considered low frequency band (frequencies below 1000 Hz), the capacitive component of tissue impedance, the inductive effect, the electromagnetic propagation effect, and thus the temporal derivatives can be neglected in the Maxwell equations of electrodynamics [26]. It can be assumed that  $\mu$  is constant over the whole volume and equal to the permeability of vacuum [26]. Therefore, the electric and magnetic fields can be described by the quasi-static Maxwell equations

$$\nabla \cdot \mathbf{D} = \rho,$$

$$\nabla \times \mathbf{E} = 0,$$

$$(3.1) \quad \nabla \times \mathbf{B} = \mu \mathbf{j},$$

$$(3.2) \quad \nabla \cdot \mathbf{B} = 0$$

with the material equations

$$\mathbf{D} = \epsilon \mathbf{E},$$

$$\mathbf{B} = \mu \mathbf{H},$$

since biological tissue mainly behaves as an electrolyte [26]: The electric field can be expressed as a negative gradient of a scalar potential:

$$(3.3) \quad \mathbf{E} = -\nabla \Phi.$$

In the field of bioelectromagnetism, the current density is divided into two parts [26], the primary or impressed current,  $\mathbf{j}^p$ , and the *secondary* or return currents,  $\underline{\underline{\sigma}}\mathbf{E}$ ,

$$(3.4) \quad \mathbf{j} = \mathbf{j}^p + \underline{\underline{\sigma}}\mathbf{E},$$

where  $\underline{\underline{\sigma}} : \Omega \rightarrow \mathbb{R}^{3 \times 3}$  denotes the  $3 \times 3$  conductivity tensor.

**3.2. The forward problem.** Taking the divergence of (3.1) (divergence of a curl of a vector is zero) and using (3.3) and (3.4) give the Poisson equation

$$(3.5) \quad \nabla \cdot (\underline{\sigma} \nabla \Phi) = \nabla \cdot \mathbf{j}^p = J^p \quad \text{in } \Omega,$$

which describes the potential distribution in the head domain  $\Omega$  due to a primary current  $\mathbf{j}^p$  in the cortex sheet of the human brain. We find homogeneous Neumann boundary conditions on the head surface  $\Gamma = \partial\Omega$ ,

$$(3.6) \quad \langle \underline{\sigma} \nabla \Phi, \mathbf{n} \rangle \Big|_{\Gamma} = 0,$$

with  $\mathbf{n}$  the unit surface normal, and a reference electrode with given potential, i.e.,

$$(3.7) \quad \Phi(x_{\text{ref}}) = 0.$$

**3.3. The primary currents.** The primary currents are movements of ions within the dendrites of the large pyramidal cells of activated regions in the cortex sheet of the human brain and at already small distances equal to the size of the activated region only the dipolar moment of the source term is visible [24]. The mathematical dipole model at position  $x_0 \in \mathbb{R}^3$  with the moment  $\mathbf{M} \in \mathbb{R}^3$  can be formulated as [22]

$$(3.8) \quad J^p(x) = \nabla \cdot \mathbf{j}^p(x) := \nabla \cdot \mathbf{M} \delta(x - x_0).$$

**3.4. The subtraction approach.** In the following, it is assumed that we can find a nonempty subdomain  $\Omega^\infty \subset \Omega$  around the source position  $x_0$  with homogeneous constant conductivity  $\underline{\sigma}^\infty$ , so that  $x_0 \in \Omega^\infty / \partial\Omega^\infty$ .

For the subtraction method, the conductivity  $\underline{\sigma}$  is then split into two parts,

$$(3.9) \quad \underline{\sigma} = \underline{\sigma}^\infty + \underline{\sigma}^{\text{corr}},$$

so that  $\underline{\sigma}^\infty$  is constant over the whole domain  $\Omega$  and  $\underline{\sigma}^{\text{corr}}$  is zero in the subdomain  $\Omega^\infty$ :  $\underline{\sigma}^{\text{corr}}(x) = 0$  for all  $x \in \Omega^\infty$ . The total potential  $\Phi$  can now be split into two parts,

$$(3.10) \quad \Phi = \Phi^\infty + \Phi^{\text{corr}},$$

where the singularity potential  $\Phi^\infty$  is defined as the solution for a dipole in an unbounded homogeneous conductor with constant conductivity  $\underline{\sigma}^\infty$ . An analytic formula for  $\Phi^\infty$  will be derived in the following. Let us first discuss the case of a homogeneous and isotropic conductivity  $\underline{\sigma}^\infty|_{\Omega^\infty} = \sigma^\infty \mathbf{Id}$ ,  $\sigma^\infty \in \mathbb{R}$ . In this case, the solution of Poisson's equation

$$(3.11) \quad \Delta \Phi^\infty = J^p / \sigma^\infty$$

can be formed analytically by use of (3.8) [26]:

$$(3.12) \quad \Phi^\infty(x) = \frac{1}{4\pi\sigma^\infty} \frac{\langle \mathbf{M}, (x - x_0) \rangle}{|x - x_0|^3}.$$

In the case that the conductivity  $\underline{\sigma}^\infty$  is homogeneous and anisotropic in  $\Omega^\infty$ , we find [12]

$$(3.13) \quad \Phi^\infty(x) = \frac{1}{4\pi\sqrt{\det \underline{\sigma}^\infty}} \frac{\langle \mathbf{M}, (\underline{\sigma}^\infty)^{-1}(x - x_0) \rangle}{\langle (\underline{\sigma}^\infty)^{-1}(x - x_0), (x - x_0) \rangle^{3/2}}.$$

In both cases the potential  $\Phi^\infty$  has a singularity at  $x = x_0$  but is smooth everywhere else. Inserting (3.9)–(3.11) into (3.5) yields a Poisson equation for the correction potential

$$(3.14) \quad -\nabla \cdot (\underline{\sigma} \nabla \Phi^{\text{corr}}) = f \quad \text{in } \Omega, \quad f := \nabla \cdot (\underline{\sigma}^{\text{corr}} \nabla \Phi^\infty),$$

with inhomogeneous Neumann boundary conditions at the surface:

$$(3.15) \quad \langle \underline{\sigma} \nabla \Phi^{\text{corr}}, \mathbf{n} \rangle = g \quad \text{on } \Gamma, \quad g := -\langle \underline{\sigma} \nabla \Phi^\infty, \mathbf{n} \rangle.$$

After solving this numerically toward  $\Phi^{\text{corr}}$ , the unknown scalar potential  $\Phi$  can then be calculated using (3.10). The gain of the reformulation using the explicit representation of  $\Phi^\infty$  is that the singularity on the right-hand side of (3.5) has been eliminated: let  $\bar{\Phi}^\infty$  denote a smooth extension of  $\Phi^\infty|_{\Omega \setminus \Omega^\infty}$  to  $\Omega$ . Then  $\bar{\Phi}^\infty$  is globally smooth and  $\underline{\sigma}^{\text{corr}} \nabla \Phi^\infty = \underline{\sigma}^{\text{corr}} \nabla \bar{\Phi}^\infty$  ( $\underline{\sigma}^{\text{corr}}$  vanishes in  $\Omega^\infty$ ), so that the right-hand side  $f$  is square-integrable over the whole domain  $\Omega$ . For the given right-hand side  $f$  and the linear operator  $\nabla \cdot \underline{\sigma} \nabla$ , we can apply a standard FE discretization and thus derive standard FE convergence results.

**3.5. Existence and uniqueness of the solution.** In the following, we use the definitions of the scalar products, norms, seminorms, function spaces, and weak derivatives as used in the FE standard literature (see, e.g., [4, 14]).

Equation (3.14) can only be understood in the classical sense under the condition  $\underline{\sigma} \in C^1(\Omega, \mathbb{R}^{3 \times 3})$ . For the multilayer model with conductivity jumps between the compartments, we search for a weak solution in the Sobolev space  $H^1(\Omega)$ .

**THEOREM 3.1** (variant of Friedrichs's inequality [4]). *Let  $\Omega$  be a domain with volume  $\mu(\Omega)$  that is contained in a cube with edge length  $s$ . We then find for all  $u \in H^1(\Omega)$*

$$\|u\|_0 \leq |\bar{u}| \sqrt{\mu(\Omega)} + 2s \|u\|_1, \quad \bar{u} := \int_{\Omega} u(x) dx / \mu(\Omega).$$

For existence and uniqueness of a solution for the correction potential, we will make use of the following specific subspace of  $H^1(\Omega)$ :

$$H_*^1(\Omega) := \left\{ v \in H^1(\Omega) \mid \int_{\Omega} v(x) dx = 0 \right\}.$$

We now formulate the bilinear form  $a : H^1(\Omega) \times H^1(\Omega) \rightarrow \mathbb{R}$  and the functional  $l : H^1(\Omega) \rightarrow \mathbb{R}$  for our application:

$$(3.16) \quad a(u, v) := \int_{\Omega} \langle \underline{\sigma}(x) \nabla u(x), \nabla v(x) \rangle dx, \quad l(v) := \int_{\Omega} f(x) v(x) dx + \int_{\Gamma} g v d\Gamma,$$

with  $f$  and  $g$  from (3.14) and (3.15).

**DEFINITION 3.2** (continuous bilinear form). *Let  $H$  be a Hilbert space. A bilinear form  $\mathcal{B} : H \times H \rightarrow \mathbb{R}$  is called continuous if there is a constant  $C_{\text{cont}} > 0$ , so that*

$$\forall u, v \in H : \quad |\mathcal{B}(u, v)| \leq C_{\text{cont}} \|u\|_H \|v\|_H.$$

**LEMMA 3.3.** *The bilinear form  $a(\cdot, \cdot)$  from (3.16) is continuous on  $H^1(\Omega) \times H^1(\Omega)$ .*

*Proof.* Let  $\sigma_{max}$  be the largest eigenvalue of any conductivity tensor  $\underline{\sigma}(x)$ ,  $x \in \Omega$ . Then the bilinear form is continuous,

$$\begin{aligned} |a(u, v)| &\stackrel{(3.16)}{=} \left| \int_{\Omega} \langle \underline{\sigma}(x) \nabla u(x), \nabla v(x) \rangle dx \right| \leq \sigma_{max} \int_{\Omega} \|\nabla u(x)\| \|\nabla v(x)\| dx \\ &\stackrel{\text{H\"older}}{\leq} \sigma_{max} \|\nabla u\|_{L^2(\Omega)} \|\nabla v\|_{L^2(\Omega)} \leq \sigma_{max} \|u\|_{H^1(\Omega)} \|v\|_{H^1(\Omega)}, \end{aligned}$$

with continuity constant  $C_{\text{cont}} = \sigma_{max}$ .  $\square$

DEFINITION 3.4 (*H-ellipticity*). A symmetric, continuous bilinear form  $\mathcal{B}$  is called *H-elliptic* if there is a constant  $C_{\text{ell}} > 0$  so that

$$\forall u \in H : \quad \mathcal{B}(u, u) \geq C_{\text{ell}} \|u\|_H^2.$$

LEMMA 3.5. The bilinear form  $a(\cdot, \cdot)$  from (3.16) is  $H_*^1(\Omega)$ -elliptic.

*Proof.* Let  $\sigma_{min}$  be the smallest eigenvalue of any conductivity tensor  $\underline{\sigma}(x)$ ,  $x \in \Omega$ . Let  $u \in H_*^1(\Omega)$ , and let  $s$  be the constant from Friedrichs's inequality. Then the ellipticity

$$\begin{aligned} a(u, u) &= \int_{\Omega} \langle \underline{\sigma}(x) \nabla u(x), \nabla u(x) \rangle dx \geq \sigma_{min} \int_{\Omega} \langle \nabla u(x), \nabla u(x) \rangle dx = \sigma_{min} |u|_1^2 \\ &= \frac{\sigma_{min}}{1 + 4s^2} (|u|_1^2 + 4s^2 |u|_1^2) \stackrel{|\bar{u}|=0}{=} \frac{\sigma_{min}}{1 + 4s^2} (|u|_1^2 + (|\bar{u}| \sqrt{\mu(\Omega)} + 2s |u|_1)^2) \\ &\stackrel{\text{Th. 3.1}}{\geq} \frac{\sigma_{min}}{1 + 4s^2} (|u|_1^2 + \|u\|_0^2) = \frac{\sigma_{min}}{1 + 4s^2} \|u\|_1^2 \end{aligned}$$

holds with ellipticity constant  $C_{\text{ell}} = \sigma_{min}/(1 + 4s^2)$ .  $\square$

LEMMA 3.6. The functional  $l(\cdot)$  in (3.16) is well defined and bounded on  $H^1(\Omega)$ , particularly  $l(\cdot) \in (H_*^1(\Omega))'$ .

THEOREM 3.7 (existence and uniqueness). Let  $\Omega$  be compact with piecewise smooth boundary (e.g., polygonal). Then the variational problem

$$\text{seek } u \in H_*^1(\Omega) : \quad \forall v \in H^1(\Omega), \quad a(u, v) = l(v)$$

has exactly one solution  $u \in H_*^1(\Omega)$ .

*Proof.* The bilinear form  $a(\cdot, \cdot)$  is  $H^1$ -continuous (Lemma 3.3) and  $H_*^1(\Omega)$ -elliptic (Lemma 3.5) and the functional  $l(\cdot)$  is bounded (Lemma 3.6). Due to Lax–Milgram we find exactly one  $u \in H_*^1(\Omega)$  that solves the variational problem for all  $v \in H_*^1(\Omega)$ . For  $\tilde{v} \in H^1(\Omega)$  we use the splitting  $\tilde{v} = v + c \cdot 1$ ,  $v \in H_*^1(\Omega)$ , and find that first

$$a(u, \tilde{v}) = a(u, v) + c \cdot a(u, 1) = a(u, v)$$

and, with  $\Omega' := \Omega \setminus K(x_0, \epsilon)$  ( $K(x_0, \epsilon)$  being a small ball with radius  $\epsilon$  around the

source position at  $x_0$ ),

$$\begin{aligned}
l(\tilde{v}) &= l(v) + c \cdot l(1) = l(v) + c \cdot \left( \int_{\Omega} f + \int_{\Gamma} g \right) \\
&= l(v) + c \cdot \left( \int_{\Omega} \nabla \cdot (\underline{\underline{\sigma}}^{\text{corr}} \nabla \Phi^{\infty}) - \int_{\Gamma} \langle \underline{\underline{\sigma}} \nabla \Phi^{\infty}, \mathbf{n} \rangle \right) \\
&\stackrel{\text{Gau\ss}}{=} l(v) + c \cdot \left( \int_{\Gamma} \langle \underline{\underline{\sigma}}^{\text{corr}} \nabla \Phi^{\infty}, \mathbf{n} \rangle - \int_{\Gamma} \langle \underline{\underline{\sigma}} \nabla \Phi^{\infty}, \mathbf{n} \rangle \right) \\
&= l(v) - c \int_{\Gamma} \langle \underline{\underline{\sigma}}^{\infty} \nabla \Phi^{\infty}, \mathbf{n} \rangle \\
&\stackrel{\text{Gau\ss}}{=} l(v) - c \left( \int_{\Omega'} \nabla \cdot (\underline{\underline{\sigma}}^{\infty} \nabla \Phi^{\infty}) - \int_{\partial K(x_0, \epsilon)} \langle \underline{\underline{\sigma}}^{\infty} \nabla \Phi^{\infty}, \mathbf{n} \rangle \right) \\
&= l(v).
\end{aligned}$$

In the last step of the above equation, both integrals are zero: The volume integral is zero, because  $\Phi^{\infty}$  defined in (3.12) or (3.13) is a solution of the homogeneous problem and  $J^p(x) = 0$  for all  $x \in \Omega'$ . The surface integral is zero, because  $\Phi^{\infty}$  is the potential for a dipole in the center of the spherical integration domain, and, when dividing the domain into two half-spheres, the surface integral over the one is exactly the negative of the other.  $\square$

**3.6. FE formulation and implementation issues.** A numerical method is needed for the field simulation in a realistically shaped head volume conductor. We will use the FE method because of its ability to treat geometries of arbitrary shape and inhomogeneous and anisotropic material parameters. As a first step, we will use partial integration on the right-hand side of (3.14) (see (3.14), (3.15), and (3.16)):

$$(3.17) \quad l(v) = - \int_{\Omega} \langle \nabla v(x), \underline{\underline{\sigma}}^{\text{corr}}(x) \nabla \Phi^{\infty}(x) \rangle dx - \int_{\Gamma} \langle \underline{\underline{\sigma}}^{\infty} \nabla \Phi^{\infty}(x), \mathbf{n}(x) \rangle v(x) dx.$$

The linear space  $H^1(\Omega)$  is discretized by the FE space

$$V_N := \text{span}\{\varphi_i(x) \mid i = 1, \dots, N\} \subset H^1(\Omega)$$

spanned by piecewise affine basis functions  $\varphi_i$  at nodes  $\xi_i$ , i.e.,  $\varphi_i(x) = 1$  for  $x = \xi_i$  and  $\varphi_j(x) = 0$  for all  $j \neq i$ . The singularity potential  $\Phi^{\infty}$  can be projected into this FE space (required only in the smooth part  $\Omega \setminus \Omega_{\infty}$ ):

$$(3.18) \quad \Phi^{\infty}(x) \approx \Phi_h^{\infty}(x) := \sum_{i=1}^N \varphi_i(x) u_i^{\infty}, \quad u_i^{\infty} := \Phi^{\infty}(\xi_i).$$

Now we seek coefficients  $u_j$  for the discrete approximation of  $\Phi^{\text{corr}}(x) \approx \Phi_h^{\text{corr}}(x) := \sum_{j=1}^N \varphi_j(x) u_j$ ; i.e., we solve the problem

$$\text{find } u \in H^1(\Omega) \text{ so that } \forall v \in H^1(\Omega) : \quad a(u, v) = l(v)$$

in the discrete space  $V_N$ :

$$(3.19) \quad \text{find } u \in V_N \text{ so that } \forall v \in V_N : \quad a(u, v) = l(v).$$

The coefficient vector  $\underline{u} := (u_1, \dots, u_N)$  solves the corresponding linear system

$$(3.20) \quad K\underline{u} = \underline{j}^\infty, \quad \underline{j}^\infty := -K^{\text{corr}}\underline{u}^\infty - S\underline{u}^\infty,$$

where  $\underline{u}^\infty := (u_1^\infty, \dots, u_N^\infty)$  is the coefficient vector for  $\Phi_h^\infty$  and

$$\begin{aligned} K_{i,j} &:= \int_{\Omega} \langle \underline{\sigma}(x) \nabla \varphi_i(x), \nabla \varphi_j(x) \rangle dx, \\ K_{i,j}^{\text{corr}} &:= \int_{\Omega} \langle \underline{\sigma}^{\text{corr}}(x) \nabla \varphi_i(x), \nabla \varphi_j(x) \rangle dx, \\ S_{i,j} &:= \int_{\Gamma} \langle \underline{\sigma}^\infty(x) \nabla \varphi_j(x), \mathbf{n}(x) \rangle \varphi_i(x) d\Gamma x. \end{aligned}$$

The computation of the matrix entries is simple, because the gradients of the basis functions are piecewise constant. We used the template C++ library COLSAMM described in detail in [8]. Additionally, the supports of the basis functions are small and local so that the number of entries in  $K, K^{\text{corr}}, S$  is  $\mathcal{O}(N)$ .

In the next section we will see that the  $L^2$ -error of the approximation

$$\varepsilon_N := \|\Phi_h^{\text{corr}} - \Phi^{\text{corr}}\|_{L^2(\Omega)}$$

behaves like  $h^2 = N^{-2/3}$ , so we have to use a finite dimensional but large space  $V_N$ . In order to solve the large linear system (3.20) for the correction potential, we apply an AMG-CG solver [13, 31]. For the special case of a homogeneous conductivity  $\underline{\sigma}^\infty$  in the source area (the cortex), it was shown in [32] that one can compute lead field bases for EEG and MEG which then strongly reduce the computational burden for the FE-based inverse problem in EEG and MEG.

**3.7. Convergence analysis.** For our FE approximation  $\Phi_h^{\text{corr}}$ , we are interested in estimates of the form

$$(3.21) \quad \|\Phi^{\text{corr}} - \Phi_h^{\text{corr}}\| \leq Ch^k$$

with the largest possible quantitative order  $k$ .  $h$  denotes the edge length of a finite element. In general, the order depends on the regularity of the solution, on the degree of the FE trial-functions, on the chosen Sobolev norm, and on the approximation properties of the triangulation to the geometry.

For a one-layer model with homogeneous conductivity, we have the following property.

**THEOREM 3.8** (quantitative error estimate for one-layer model [14]). *Let us assume a sufficiently regular solution  $\Phi^{\text{corr}} \in H^2(\Omega)$ . For an appropriate triangulation (hexahedrization), linear (trilinear) FE trial-functions, and a continuous and elliptic bilinear form  $a(\cdot, \cdot)$ , we find a constant  $C_1$  which is independent of  $\Phi^{\text{corr}}$  and  $h$  with*

$$\|\Phi^{\text{corr}} - \Phi_h^{\text{corr}}\|_1 \leq C_1 h \|\Phi^{\text{corr}}\|_2.$$

The regularity assumption  $\Phi^{\text{corr}} \in H^2(\Omega)$  is typically fulfilled because the boundary of the domain  $\Omega$  is piecewise smooth.

**LEMMA 3.9** (Aubin–Nitsche [14]). *Let us assume a sufficiently regular solution  $\Phi^{\text{corr}} \in H^2(\Omega)$ . For an appropriate triangulation (hexahedrization), linear (trilinear) FE trial-functions, and a continuous and elliptic bilinear form  $a(\cdot, \cdot)$ , we find a constant  $C_2$  which is independent of  $\Phi^{\text{corr}}$  and  $h$  with*

$$\|\Phi^{\text{corr}} - \Phi_h^{\text{corr}}\|_0 \leq C_2 h^2 \|\Phi^{\text{corr}}\|_2.$$

For a multilayer model with different conductivities on each compartment, we can only assume  $\Phi^{\text{corr}} \in H^1(\Omega)$ . Following Hackbusch [14], we can hope that the general error bounds  $\|\Phi^{\text{corr}} - \Phi_h^{\text{corr}}\|_1 = \mathcal{O}(h)$  and  $\|\Phi^{\text{corr}} - \Phi_h^{\text{corr}}\|_0 = \mathcal{O}(h^2)$  can be achieved by means of isoparametric, i.e., geometry conforming, finite elements.

With regard to our specific application, we can give a statement concerning the property of the constant  $C$  in (3.21), which will be of practical interest (see section 4).

LEMMA 3.10. *Let  $\delta$  be the distance between the source position  $x_0$  and the closest location of the next conductivity jump on  $\partial\Omega^\infty$ . If  $\delta$  gets small, then the constant  $C(\delta)$  in*

$$|l(v)| \leq C(\delta) \|v\|_{L_2(\Omega)} \quad \forall v \in H^1(\Omega),$$

with  $l(v)$  from (3.17), is proportional to  $\delta^{-5/2}$  ( $c_1(\delta) \approx \delta^{-5/2}$ ).

*Proof.* When defining  $r := x - x_0$ , we find  $|\Delta\Phi^\infty| \approx 1/|r|^4$  and, with  $\bar{\Omega} := \Omega \setminus \Omega^\infty$ ,

$$\|\Delta\Phi^\infty\|_{L_2(\bar{\Omega})} = \sqrt{\int_{\bar{\Omega}} (\Delta\Phi^\infty)^2 dx} \approx \sqrt{\int_{|r| \geq \delta} 1/r^8 dr} \approx \sqrt{1/\delta^5} = \delta^{-5/2} =: c_1(\delta).$$

We then find constants  $C(\delta)$  and  $c_2$ , so that

$$\begin{aligned} |l(v)| &= \left| \int_{\Omega} \nabla \cdot (\underline{\sigma}^{\text{corr}} \nabla \Phi^\infty) v dx - \int_{\Gamma} \langle \underline{\sigma} \nabla \Phi^\infty, \mathbf{n} \rangle v d\Gamma \right| \\ &\leq \int_{\Omega} |\nabla \cdot (\underline{\sigma}^{\text{corr}} \nabla \Phi^\infty) v| dx + c_2 \|v\|_{L_2(\Omega)} \\ &\leq \sigma_{\max}^{\text{corr}} \int_{\bar{\Omega}} \|\Delta\Phi^\infty\| \|v\| dx + c_2 \|v\|_{L_2(\Omega)} \\ &\stackrel{\text{H\"older}}{\leq} \sigma_{\max}^{\text{corr}} \|\Delta\Phi^\infty\|_{L_2(\bar{\Omega})} \|v\|_{L_2(\bar{\Omega})} + c_2 \|v\|_{L_2(\Omega)} \\ &\leq (\sigma_{\max}^{\text{corr}} c_1(\delta) + c_2) \|v\|_{L_2(\Omega)} \leq C(\delta) \|v\|_{L_2(\Omega)}. \quad \square \end{aligned}$$

Lemma 3.10 has to be interpreted in the following way. If the source approaches a next conductivity jump, i.e., if  $\delta$  goes to 0, then the constant for the upper estimation of the right-hand side functional  $l$  gets larger (with exponent 5/2). Because of the assumed  $H^2$ -regularity, we find [4]

$$\|\Phi^{\text{corr}} - \Phi_h^{\text{corr}}\|_0 \leq C_2 h^2 \|\Phi^{\text{corr}}\|_2 \leq C_2 h^2 \|l\|_0 \leq C(\delta) C_2 h^2.$$

For sources close to the next conductivity jump (e.g., sources with high eccentricity; see section 4), we have to be aware of possibly larger numerical errors because of a strongly increasing constant  $C(\delta)$ .

#### 4. Validation and numerical experiments.

##### 4.1. Validation in multilayer sphere models.

**4.1.1. Analytical solution.** In [23], series expansion formulas were derived for a mathematical dipole in a multilayer sphere model, denoted now as “the analytical solution.” A rough overview of the formulas will be given in this section. The model consists of shells  $S$  up to 1 with radii  $r_S < r_{S-1} < \dots < r_1$  and constant radial,  $\sigma^{\text{rad}}(r) = \sigma_j^{\text{rad}} \in \mathbb{R}^+$ , and constant tangential conductivity,  $\sigma^{\text{tang}}(r) = \sigma_j^{\text{tang}} \in \mathbb{R}^+$ , within each layer  $r_{j+1} < r < r_j$ . It is assumed that the source at position  $x_0$  with radial coordinate  $r_0 \in \mathbb{R}$  is in a more interior layer than the measurement electrode at position  $x_e \in \mathbb{R}^3$  with radial coordinate  $r_e = r_1 \in \mathbb{R}$ . The spherical harmonics expansion for the mathematical dipole (3.8) was expressed in terms of the gradient of the monopole potential with respect to the source point, using an asymptotic approximation and an addition-subtraction method to speed up the series convergence [23]. This resulted in

$$\Phi(x_0, x_e) = \frac{1}{4\pi} \left\langle \mathbf{M}, S_0 \frac{x_e}{r_e} + (S_1 - \cos \omega_{0e} S_0) \frac{x_0}{r_0} \right\rangle$$

with  $\omega_{0e}$  being the angular distance between source and electrode and with

$$(4.1) \quad S_0 = \frac{F_0}{r_0} \frac{\Lambda}{(1 - 2\Lambda \cos \omega_{0e} + \Lambda^2)^{3/2}} + \frac{1}{r_0} \sum_{n=1}^{\infty} \{(2n+1)R_n(r_0, r_e) - F_0 \Lambda^n\} P'_n(\cos \omega_{0e})$$

and

$$(4.2) \quad S_1 = F_1 \frac{\Lambda \cos \omega_{0e} - \Lambda^2}{(1 - 2\Lambda \cos \omega_{0e} + \Lambda^2)^{3/2}} + \sum_{n=1}^{\infty} \{(2n+1)R'_n(r_0, r_e) - F_1 n \Lambda^n\} P_n(\cos \omega_{0e}).$$

The coefficients  $R_n$  and their derivatives  $R'_n$  can be computed analytically and the derivative of the Legendre polynomial can be determined by means of a recursion formula. Refer to [23] for the derivation of the above series of differences and for the definition of  $F_0$ ,  $F_1$ , and  $\Lambda$ .<sup>1</sup> Here, it is important only that the latter terms can be computed from the given radii and conductivities of layers between source and electrode and of the radial coordinate of the source and that they are independent of  $n$ . The computation of the series (4.1) and (4.2) are stopped after the  $k$  term if the following criterion is fulfilled:

$$(4.3) \quad \frac{t_k}{t_0} \leq v, \quad t_k := (2k+1)R'_k - F_1 k \Lambda^k.$$

In the following simulations, a value of  $10^{-6}$  was chosen for  $v$ . Using the asymptotic expansion, no more than 30 terms were then needed for the series computation for each electrode.

**4.1.2. Model generation and error criteria.** In source reconstruction, head modeling is generally based on segmented magnetic resonance (MR) data, where curved tissue boundaries have a stair-step representation. We therefore created a

<sup>1</sup>The following is a result of a discussion with J. C. de Munck: While constants in formulas (71) and (72) in the original paper [23] have to be flipped, our versions of  $S_0$  and  $S_1$  in (4.1) and (4.2) are correct.

three-compartment sphere model ( $S = 3$  in section 4.1.1) in MR format with  $1\text{mm}^3$  voxel resolution as a basis for our validation studies. Starting from the outside, the layers represent the compartments skin, skull, and brain with outer surfaces of radii  $r_1 = 90\text{mm}$ ,  $r_2 = 80\text{mm}$ , and  $r_3 = 70\text{mm}$ , respectively. In the isotropic simulations, we chose conductivities of  $\sigma_1 = 0.33\text{ S/m}$ ,  $\sigma_2 = 0.0042\text{ S/m}$ , and  $\sigma_3 = 0.33\text{ S/m}$  for the three compartments [27], while we chose  $\sigma_2^{\text{rad}} = 0.0042\text{ S/m}$  and  $\sigma_2^{\text{tang}} = 0.042\text{ S/m}$  for the simulations with a 1:10 anisotropic skull compartment [18].

Comparisons between the numeric and the analytic solutions were made for dipoles located on the  $y$ -axis at depths of 0% to 95% (in 1mm steps) of the inner layer (70mm radius) using both radial and tangential orientations. We defined *eccentricity* as the percent ratio of the distance between the source location and the model midpoint divided by the radius of the inner sphere. As reported in [18] and further explained in the discussion, the dipoles that are located in the cortex will have an eccentricity lower than 92%. Tangential sources were oriented in the  $+z$ -axis and radial dipoles in the  $+y$ -axis. The dipole moments were 1nAm. To achieve error measures which are independent of the specific choice of the sensor configuration, we distributed electrodes in a most regular way over a given sphere surface: we generated 134 electrode configurations on the surface of the outer sphere (90mm, surface-EEG *sEEG*) and under the skull (radius 70mm, internal-EEG *iEEG*).

We used two error criteria that are commonly used in source analysis [19, 2, 18, 27]—the correlation coefficient (CC) and the magnification factor (MAG). The CC is defined as

$$(4.4) \quad \text{CC} = \frac{\sum_{i=1}^m (\Phi_i^{\text{ana}} - \bar{\Phi}^{\text{ana}})(\Phi_i^{\text{num}} - \bar{\Phi}^{\text{num}})}{\sqrt{\sum_{i=1}^m (\Phi_i^{\text{ana}} - \bar{\Phi}^{\text{ana}})^2} \sqrt{\sum_{i=1}^m (\Phi_i^{\text{num}} - \bar{\Phi}^{\text{num}})^2}},$$

where  $m$  denotes the number of sensors,  $\underline{\Phi}_{\text{ana}} \in \mathbb{R}^m$  and  $\underline{\Phi}_{\text{num}} \in \mathbb{R}^m$  the analytic or numeric solution vectors at the measurement positions, respectively, and  $\bar{\Phi}^{\text{ana}}$  and  $\bar{\Phi}^{\text{num}}$  the sample means. The CC is a measure for the topography error, driven primarily by changes in dipole location and orientation (minimal error:  $\text{CC} = 1$ ). The second similarity measure, the MAG, is defined as

$$(4.5) \quad \text{MAG} = \frac{\sqrt{\sum_{i=1}^m (\Phi_i^{\text{num}})^2}}{\sqrt{\sum_{i=1}^m (\Phi_i^{\text{ana}})^2}},$$

and indicates changes in the source strength (minimal error:  $\text{MAG} = 1$ ).

**4.1.3. Hexahedra mesh generation.** Our hexahedra mesh generation approach takes advantage of the spatial discretization inherent in MR images. The voxel-based approach directly converts image voxels to eight-noded hexahedra elements, so that a  $1\text{mm}^3$  FE hexahedra model (model `cube3130` in Table 4.1) exactly represents the segmented tissues. In order to keep the computation amount within a reasonable limit, our mesh generator allows a lower resolution with edge lengths of  $e$  times the edge length of a voxel-sized cube ( $e$  being an integer multiple). In this case, the generated cube is assigned the most frequent label of its  $e^3$  interior voxels.

TABLE 4.1  
Hexahedra models: Mesh description.

Model	Nodes	Elements	Mesh resolution (in mm)
cube3130	3,130,496	3,053,617	1.0 regular
cube398	397,634	378,384	2.0 regular
cube398ns	397,634	378,384	2.0 node-shift
cube52	52,138	47,272	4.0 regular

TABLE 4.2  
Tetrahedra models: Mesh description. With increasing depth, the thinning distance was increased as indicated in the table for models tet57 and tet156.

Model	Nodes	Elements	Thinning (mm)	Erosions (in mm)		
				skin	skull	brain
tet606	605,959	3,680,234	1.1	4 × 2.0	4 × 2.0	all 2.0
tet234	234,314	1,412,813	2.0	4 × 2.0	4 × 2.0	all 2.0
tet156	156,074	930,175	2.0-5.0	3.0, 4.0	3.0, 3.0, 2.0	2.0, 2.0, then 5.0
tet57	57,033	328,511	3.0-7.0	3.0, 4.0	3.0, 4.0	all 7.0

Material interfaces of regular hexahedra models are characterized by abrupt transitions and right angles. In [7], a node-shift approach was proposed for a biomechanical FE application in order to smooth the irregular boundaries, leading to a better representation of the interfaces between different tissue compartments. The node-shift hexahedra approach was used for mesh `cube398ns` in Table 4.1. The table summarizes the properties of all hexahedra models that we used for validation purposes in this study.

**4.1.4. Tetrahedra mesh generation.** For the tetrahedra meshing approach, we used the software CURRY [9] to create a surface-based tetrahedral tessellation of the segmented and auxiliary surfaces of the three-layer sphere model. The procedure exploits the Delaunay criterion, enabling the generation of compact and regular tetrahedra. In Table 4.2, we indicate the thinning-distance parameter, which is used for the computation of FE vertices on the segmented and auxiliary surfaces. Furthermore, the erosion parameters for defining intermediate auxiliary surfaces within each layer are shown. As an example, for model `tet156` in Table 4.2, we have used a thinning of 2mm for the compartments skin and skull and increased the thinning distance to maximally 5mm within the brain compartment. We furthermore used skin surface erosions of 3.0 and 4.0mm to generate auxiliary surfaces at 87 and 83mm for the skin compartment and auxiliary surfaces of 77, 74, and 72mm for the skull compartment before tetrahedra mesh generation.

**4.1.5. Isotropic three-layer sphere modeling.** Figure 4.1 plots CC and MAG for the total surface potentials at 134 sEEG measurement electrodes on the outer surface ( $r_1 = 90\text{mm}$ ) for the different source eccentricities. The performance of the subtraction method is completely satisfying for model `cube3130` and `cube398ns`, with a CC of 0.999 or better and a MAG of 1.028 or better at all depths and for both source orientations. For high eccentricities, the errors begin to rise—a behavior which has also been observed in [27] in a regular 1mm hexahedra model. For the 2mm regular cube model `cube398`, we also get very satisfying CC results, while, due to the stair-step approximation of the compartment boundaries, we face about 10% MAG error over the whole range of eccentricities. This magnitude problem, which is a consequence of the rough geometry description, can be alleviated with the node-shift approach, where, with maximally 1.6% for model `cube398ns`, we achieve the smallest

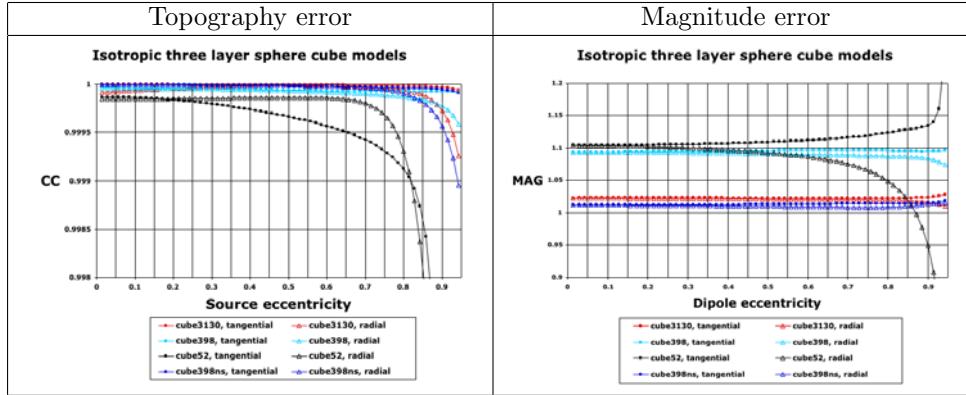


FIG. 4.1. *Isotropic three compartment sphere model: Numerical accuracy for hexahedra models at 134 sEEG electrodes.*

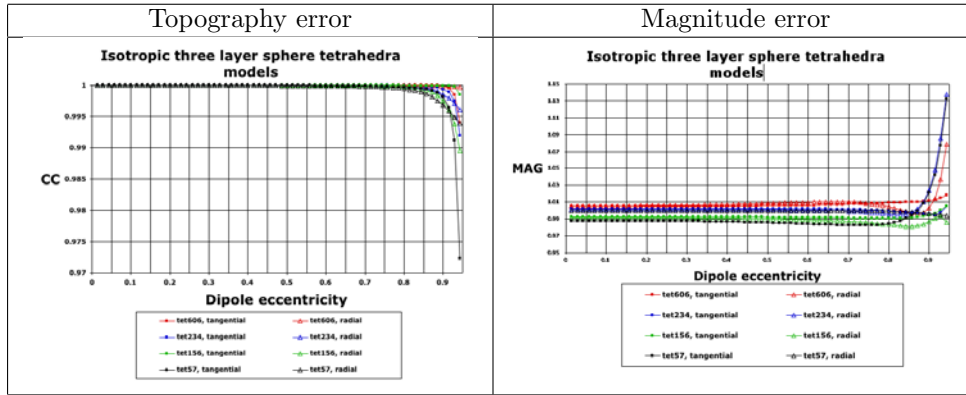


FIG. 4.2. *Isotropic three compartment sphere model: Numerical accuracy for tetrahedra models at 134 sEEG electrodes.*

MAG errors of all tested hexahedra models. Model `cube52` is too coarse to appropriately represent the volume conductor. Even if sufficient CC accuracies are achieved for eccentricities up to 90% and therefore for the vast majority of realistic source positions, the results for higher eccentricities fall below a CC of 0.99, and also the MAG is equipped with an error of up to 26%.

Figure 4.2 shows the sEEG ( $r_1 = 90\text{mm}$ ) similarity measures CC and MAG for the tetrahedra models for the different source eccentricities. We observe larger topography errors and sharper declines at high eccentricities than for the best hexahedra models (note the different CC scalings in Figures 4.1 and 4.2), but with a CC of 0.99 or better, the performance of the subtraction method over the whole range of practically interesting eccentricities is still satisfying for most of the examined models. Even the coarsest model `tet57` gives sufficient CC accuracies for eccentricities up to 94%, but the CC then declines strongly below a value of 0.99 for the highest evaluated eccentricity. With regard to the potential magnitude, with a maximal MAG error of 1.9% over all eccentricities and for both source orientations, the best result is achieved with model `tet156`.

#### 4.1.6. Three-layer sphere models with anisotropic skull compartment.

The importance of well-defined skull conductivity tensor eigenvectors was already pointed out in [18]. For anisotropy modeling of the middle (“skull”) compartment in a three-layer sphere model, the conductivity tensor eigenvector in a radial direction can be determined by means of normalizing the vector from an element barycenter to the midpoint of the sphere model, denoted now as the *optimal sphere procedure*. The vector product can then be used to define both tangential directions. With regard to a realistic head model, we also evaluated another procedure. We eroded the segmented outer surface of the middle “skull” compartment by half of the “skull’s” thickness, strongly smoothed (important only in the case of a realistic head model) and triangulated it with an edge length of  $x$  mm (denoted now as the smooth surface model (SSM) *SSMx*). We then exploited the SSM surface normals for the definition of the radial tensor direction. Because the triangulated mesh is generated from a staircase-like surface, it is obvious that the edge length of the mesh should not be chosen too small. We evaluated CC and MAG in a model with 1 to 10 radial to tangential skull anisotropy when using SSM2, SSM5, SSM10, SSM20, and the optimal sphere procedure. In Figure 4.3, results are presented for SSM10, which, besides the optimal sphere procedure, led to the smallest errors. As the figure shows, the results are similar to the results in the isotropic volume conductor. Model `cube398ns` again overall performs best with a CC of more than 0.999 and a MAG of maximally 4.3%.

In a last examination, we plotted the exactness of the numerical approach versus the relative solver accuracy of the AMG-CG for the correction potential for different source eccentricities. The AMG-CG solver process was stopped if the relative error in the controllable  $K_h C_h^{-1} K_h$ -energy norm (with  $C_h^{-1}$  being one V-cycle of the AMG) was below the value indicated on the  $x$ -axis (for further information, see [31]). Errors at 134 sEEG (90mm) and at 134 iEEG (70mm) electrodes are shown in Figure 4.4. It can be observed that the higher the eccentricity of the source, the more important it is to accurately determine the correction potential. A relative solver accuracy of  $10^{-4}$  was sufficient for the tested eccentricities; the solution exactness no longer increased with higher relative solver accuracies.

**4.2. Validation in a realistic anisotropic head model.** A three tissue realistic head model with compartments skin, skull, and brain and an isotropic voxel size of  $1\text{mm}^3$  was segmented from a T1- and proton-density-weighted MR dataset of a healthy 32 year old male subject. The bimodal MR approach allowed an improved modeling of the skullshape as described in detail in [34]. 71 electrodes were positioned on the model surface using the international 10/20 system.

The model was then meshed using the different mesh generation approaches described in sections 4.1.3 and 4.1.4. Table 4.3 summarizes the parametrization of the different meshes. For hexahedra model `cube386ns`, a node-shift was used at the compartment boundaries skin, outer skull, and inner skull. For tetrahedra model `tet265`, the following surfaces were included in the meshing procedure as also indicated in Table 4.3: skin, 2mm eroded skin, outer skull, 2mm eroded outer skull, inner skull, and continuous 2mm erosions into the depths. Following the results of section 4.1.6, a strongly smoothed triangular mesh with 10mm edge length (SSM10) from a 3mm eroded outer skull surface was used for the modeling of 1 to 10 quasi-radial to quasi-tangential skull conductivity anisotropy. While, in a multilayer sphere model, CC and MAG errors for the numerically computed potential distribution serve for indirect validation of the modeled skull conductivity tensors, those error metrics are not available in a realistic head model. It is therefore important to at least visualize the

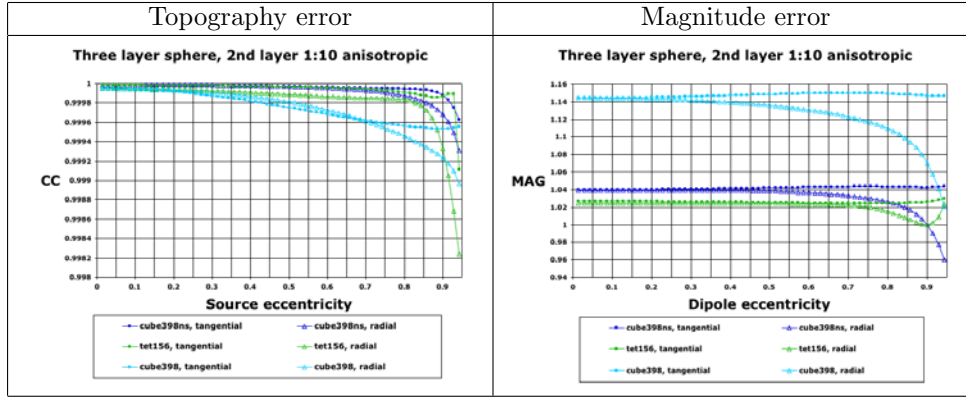


FIG. 4.3. Three compartment sphere model with a 1:10 anisotropic middle (“skull”) layer: Numerical accuracy at 134 sEEG electrodes for hexahedra models cube398ns and cube398 and tetrahedra model tet156 when using SSM10 for the determination of the “skull” conductivity tensor eigenvectors.

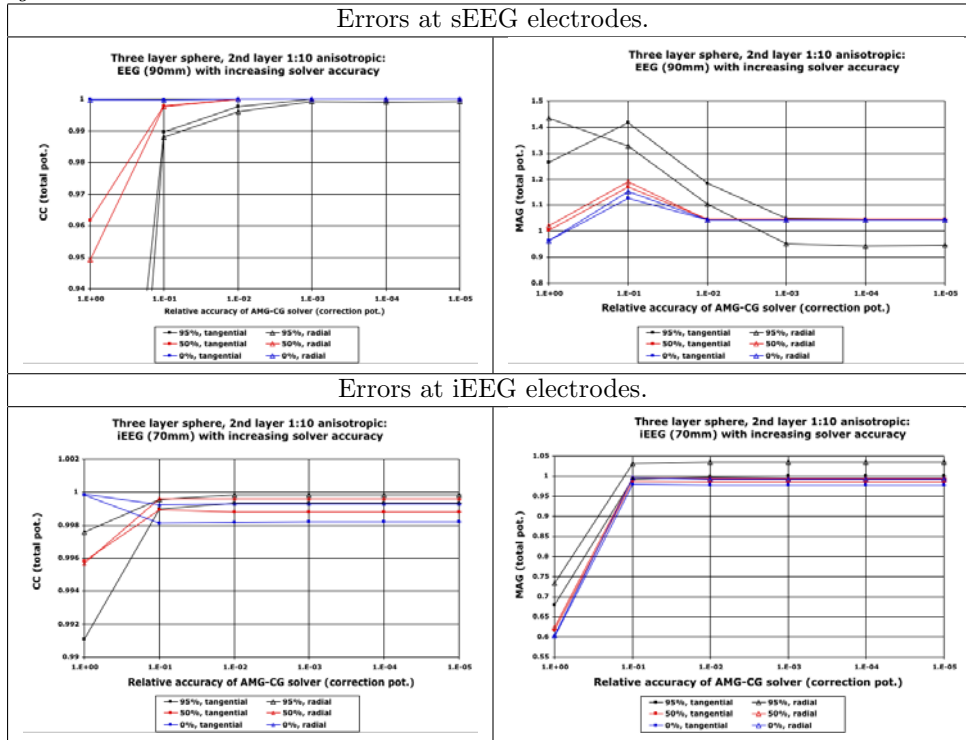


FIG. 4.4. Three compartment sphere model with a 1:10 anisotropic middle (“skull”) layer, FE model cube398ns: CC (left) and MAG (right) error at 134 sEEG electrodes on “skin” surface  $r_1 = 90\text{mm}$  (top) and at 134 iEEG electrodes on “inner skull” surface  $r_3 = 70\text{mm}$  (bottom) with increasing AMG-CG relative solver accuracy for sources at 95%, 50%, and 0% eccentricity.

tensors in order to check for correct skull tensor registration and eigenvector directions. Figure 4.5 shows the anisotropic conductivity tensor ellipsoids of the human skull compartment with the underlying T1-MRI. The figure shows that the ellipsoids are oblate with minor axis in a quasi-radial direction through the skull compartment.

TABLE 4.3  
Realistically shaped three compartment head models: Mesh description.

Model	Nodes	Elements	Thinning (in mm)	Resolution (in mm)		
				skin	skull	brain
cube386ns	385,901	366,043	2.0	2.0ns	2.0ns	2.0ns
cube386	385,901	366,043	2.0	2.0	2.0	2.0
tet265	265,313	1,620,794	1.8	2.0, rest	2.0, rest	all 2.0

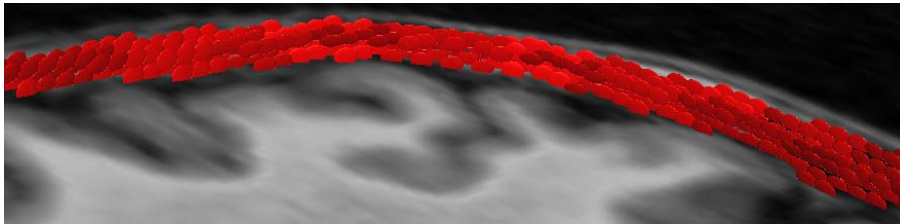


FIG. 4.5. 1:10 (Quasi-radial to quasi-tangential) anisotropic conductivity tensor ellipsoids of the human skull compartment when using SSM10 with underlying T1-MRI. Visualization, carried out using BioPSE [3], is important to validate if the ellipsoids are oblate with minor axis in a quasi-radial direction through the skull compartment.

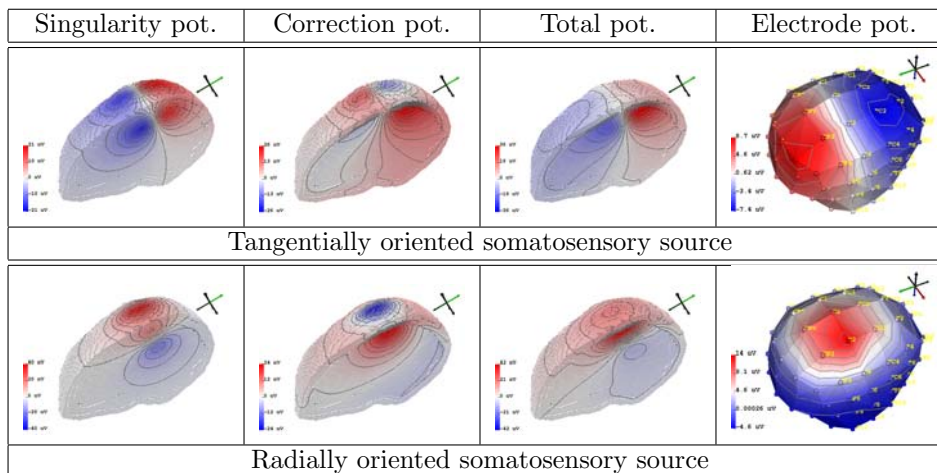


FIG. 4.6. Realistically shaped head model cube386ns with 1 to 10 quasi-radial to quasi-tangential anisotropic skull compartment: Visualization results for the singularity potential, the correction potential, and the total potential in the volume conductor and at the 71 surface electrodes for a quasi-tangentially and a quasi-radially oriented source in the somatosensory cortex. Visualization was carried out using BioPSE [3].

In a first study, we computed the singularity, the correction, and the total potential in model cube386ns for a radially and a tangentially oriented source at an eccentric location in the somatosensory cortex. Figure 4.6 presents the visualization results.

We then compared the results for the different mesh generation techniques. As the node-shifted hexahedra model showed the best accuracies in the three-layer sphere validations, we chose this model as a reference. In Table 4.4 we present the differences from the solutions in other models. With a CC above 0.998 and a maximal MAG of 6.9%, the differences among the three models are fairly small. Again, the regular

TABLE 4.4

Realistic three compartment head models, comparison of results using different meshing techniques: Differences between the forward computations at 71 electrodes using the subtraction approach for an eccentric source in the somatosensory cortex. The reference results are the ones in the node-shifted 2mm cube model, because this model performed best in the sphere validation studies.

Model	Differences for somatosensory source			
	Tangential		Radial	
	CC	MAG	CC	MAG
cube386	0.9989	1.0643	0.9982	1.0689
tet265	0.9997	1.0009	0.9997	0.9849

TABLE 4.5

Realistic volume conductor modeling: Computation times (see (3.20)) and maximal memory usage. (a) Has to be done once per head geometry. (b) Following [32], this has to be done  $\max(\text{nb\_sour}, \text{nb\_sens})$  times. (c) Has to be done  $\text{nb\_sour}$  times.

Model	Computation times (in sec.)					Max. mem.
	(a)			(b)	(c)	
	$K, K^{\text{corr}}$	$S$	AMG setup	$K\underline{u} = \underline{j}^\infty$	$\underline{u}^\infty$	
cube386ns	17.2	14.8	16.6	6.2	0.3	795MB
tet265	28.1	40.3	8.2	3.6	0.14	675MB

2mm hexahedra model `cube386` exhibits the highest magnitude difference because of its rough approximation of the interfaces.

In a final study, the computation times and the maximal amount of memory in our current implementation were measured for models `cube386ns` and `tet265` (Table 4.5). In Table 4.5, `nb_sour` is the number of sources and `nb_sens` the number of measurement sensors. The experiment was run on a Linux-PC with an Intel Pentium 4 processor (3GHz). The computation time for  $S$  contains the times for finding the source element (determination of  $\underline{\sigma}^\infty$ ), for determining surface finite elements, and for computing the integration over all surface elements. For the determination of a surface element, the property was used that it has at least one face that is not a face to any other element. A list structure was therefore built up where, for each mesh node, all neighboring finite elements were administered. A face of an element is then a face of the surface of the volume conductor if the intersection of the finite elements of all face nodes is just a single finite element. For the AMG-CG, the relative solver accuracy was chosen to be  $10^{-4}$ . The multiplication of a sparse matrix times a fully populated vector as for  $-(K^{\text{corr}} + S)\underline{u}^\infty$  in (3.20) can be neglected (0.03 sec. for `cube386ns` and 0.02 sec. for `tet265`).

With regard to the inverse problem, the computation of  $K$ ,  $K^{\text{corr}}$ , and  $S$  and the setup of the AMG preconditioner have to be carried out only once per head geometry. `nb_sour` is generally by far larger than `nb_sens` and the lead-field basis approach should be applied [32]. It reduces the necessary computation to mainly `nb_sens` times the solution of an equation system of the form  $K\underline{q} = \underline{p}$  with a fully populated right-hand side vector  $\underline{p}$  (Table 4.5 (b)) to build the lead-field basis  $B_{\text{eg}}^\infty$ , a fully populated matrix with `nb_sens`–1 rows and  $N$  columns. Each forward computation then involves only the computation of  $\underline{u}^\infty$  (Table 4.5 (c)) and its multiplication with the lead-field basis, i.e.,  $B_{\text{eg}}^\infty \underline{u}^\infty$  (0.68 sec. for model `cube386ns` and 0.47 sec. for model `tet265`).

**5. Discussion.** In this paper, we presented the theory of the subtraction approach to model a point dipole in the finite element (FE) method based electroencephalography (EEG) source reconstruction for isotropic and anisotropic volume con-

ductors. We proved existence and uniqueness of a weak solution for the potential in zero-mean function space. We embedded our numerical approach for the correction potential in the general FE convergence theory and showed that the constant in the FE convergence proof largely depends on the distance of the source to the next conductivity jump. Therefore, higher FE trial-functions or, if linear trial-functions are used, a higher integration order and/or multiple element layers are needed between the source and the next conductivity jump; otherwise one would have to be aware of probably larger and unacceptable numerical errors. Since the magnetoencephalography (MEG) forward problem is also based on the computed electric potential (see, e.g., [32]), our results are also applicable to MEG source reconstruction. Besides the presented clear mathematical theory, a further important advantage of the subtraction approach is the fact that, as soon as the corresponding singularity potential function is known, the implementation of any other primary source model is straightforward. Our theoretical statements are thus valid for any such primary source model. Despite the fact that the bioelectric primary current sources in EEG and MEG are naturally continuous throughout the cortical tissue (which would also reduce numerical errors), they are usually modeled with a mathematical point dipole [22, 24].

The main aim of our study was therefore to validate the subtraction approach for the usual model, i.e., a point current dipole in a three-layer sphere with piecewise homogeneous conductivity, for which series expansion formulas are available [23]. As a measure of similarity, we used two common criteria [19, 6]: The first and by far more important one, the correlation coefficient (CC), indicates defects in the topography of the potential distribution and therefore, with regard to the inverse solution, defects in the localization and orientation of the sources. Another frequently used topography error measure is the relative difference measure (RDM), introduced in [19]. For the used zero-mean data, CC and RDM can be related through  $RDM = \sqrt{2(1 - CC)}$ , and a CC above 0.99 has been associated with a localization error of no more than 1mm, while a CC of 0.98 led to dipole localization errors of 5–8mm on average, maximally 1.5cm [27]. In source localization practice, an accuracy of 1mm is more than satisfactory because main limitations are then due to other sources of error such as the limited data signal-to-noise ratio, segmentation errors, inaccuracies in the determination of the conductivities, etc. The second error measure, the magnification factor (MAG), indicates changes in the potential amplitude and thus in the source strength. In our sphere validation studies, we placed dipole sources at positions along the  $y$ -axes from the center of the model in 1mm steps toward the inner skull surface up to an eccentricity of 95%. As reported in [18], the dipoles that are located in the cortex will have an eccentricity lower than 92%. The reasons are that first, compartments such as the arachnoid cavity, the subdural cavity, and the dura mater, whose conductivities are generally approximated with the conductivity of the brain compartment [5, 6, 18], are located between the cortex and the inner skull surface, and second, the dipoles are located some millimeters below the cortical surface (see, e.g., [24]). Our validation has been carried out for two different classes of elements, FE hexahedra and tetrahedra. In the class of hexahedra, we examined regular and geometry-conforming node-shifted elements.

With a CC of 0.998 or better over the whole range of realistic eccentricities at the 134 regularly distributed surface or depths electrodes, we achieved completely satisfying results for all tested 1mm and 2mm isotropic and anisotropic hexahedra models. The node-shift reduced the maximal MAG error for the 2mm anisotropic model from about 15% to only 4.3%. For the tetrahedra models, we observed larger

topography errors and sharper declines at high eccentricities, but with minimal CC values of 0.99 for the whole range of tested eccentricities, the three models with higher resolutions still perform sufficiently well. In summary, with regard to the accuracy and computational complexity, the 2mm node-shifted hexahedra model achieved the best results. We found that with increasing eccentricity, a higher relative solver accuracy is needed for the correction potential, a relative accuracy of  $10^{-4}$  being sufficient for the used AMG-CG approach. Using eccentric sources in human somatosensory cortex in a realistically shaped three-compartment head model with anisotropic skull compartment, we computed the potential distributions within the volume conductor. Validation was carried out by visually inspecting and comparing the results when using the different meshing techniques.

It is well known (and, in this paper, we have given a theoretical reasoning for this fact), that with increasing eccentricity, the numerical accuracy in sphere model validations decreases, especially with regard to radially oriented dipoles [2, 5, 18]. This is the case not only for the subtraction approach in FE modeling, but also for the direct approach in FE modeling [36, 6, 16, 21] and in boundary element modeling (see, e.g., [10]). In [2, 5, 18], coarser tetrahedra mesh resolutions were considered so that larger numerical errors resulted with CCs below 0.98 for radial dipoles with eccentricities above 90%. In [2, 5], local mesh refinement was used to achieve acceptable results for all realistic eccentricities. Nevertheless, with regard to the inverse problem, the setup of source-location dependent locally refined meshes is difficult to implement and time-consuming to compute and thus might not be practical for an inverse source analysis. We propose to use a single mesh that is sufficiently fine and that resolves the geometry. For the efficient solution of the inverse problem the lead-field bases concept can then be used [32]. As shown in [31], the amount of work for the computation of the lead-field bases can be reduced by means of an AMG-CG solver.

In subsequent studies, we will perform profound comparisons of the subtraction approach with the diverse direct methods [36, 6, 30, 27, 21] for the computation of the EEG and MEG inverse problems both in anisotropic sphere models as well as in realistic anisotropic head volume conductors in order to gain deeper insight into the advantages and disadvantages of our new approach. A first comparison of the subtraction method with a direct potential approach using partial integration [30, 21] and with a direct potential approach using the principle of Saint Venant [6] can be found in [35]. As shown in the theory section of this paper, the subtraction approach enables the inclusion of local anisotropy in the source area. It is well known that the human cortex is about 1:2 anisotropic and that both EEG and MEG forward problems are especially sensitive toward local conductivity changes [16, 33]. As a final note, instead of trying to reduce numerical errors for the probably “over-singular” mathematical point dipole, it is important to reconsider other and especially smoother source models, taking into account the fact that the primary current sources are continuous throughout the cortical tissue [28, 24]. This is where the FE-based subtraction method might provide a further important contribution to EEG and MEG source analyses.

**Acknowledgments.** The authors would like to thank U. Rude, C. Pantev, S. Borm, A. Anwander, R. S. MacLeod, and C. R. Johnson for their support and the many important and helpful comments. We are especially grateful to J. C. de Munck for providing his software for the analytical solution and for his quick responses whenever needed and to the referees and the associate editor for improving our manuscript.

## REFERENCES

- [1] K. A. AWADA, D. R. JACKSON, J. T. WILLIAMS, D. R. WILTON, S. B. BAUMANN, AND A. C. PAPANICOLAOU, *Computational aspects of finite element modeling in EEG source localization*, IEEE Trans. Biomed. Engrg., 44 (1997), pp. 736–751.
- [2] O. BERTRAND, M. THÉVENET, AND F. PERRIN, *3D finite element method in brain electrical activity studies*, in Biomagnetic Localization and 3D Modeling, J. Nenonen, H. M. Rajala, and T. Katila, eds., Tech. rep., Department of Technical Physics, Helsinki University of Technology, Otaniemi, Finland, 1991, pp. 154–171.
- [3] BIOPSE, *Problem Solving Environment for Modeling, Simulation, and Visualization of Bioelectric Fields*, Scientific Computing and Imaging Institute (SCI), Salt Lake City, UT, 2002, <http://software.sci.utah.edu/biopse.html>.
- [4] D. BRAESS, *Finite Elements: Theory, Fast Solvers and Applications in Solid Mechanics*, Cambridge University Press, Cambridge, UK, 2001.
- [5] S. P. VAN DEN BROEK, *Volume Conduction Effects in EEG and MEG*, Proefschrift, Universiteit Twente, Enschede, The Netherlands, 1997.
- [6] H. BUCHNER, G. KNOLL, M. FUCHS, A. RIENÄCKER, R. BECKMANN, M. WAGNER, J. SILNY, AND J. PESCH, *Inverse localization of electric dipole current sources in finite element models of the human head*, Electroenc. Clin. Neurophysiol., 102 (1997), pp. 267–278.
- [7] D. CAMACHO, R. HOPPER, G. LIN, AND B. MYERS, *An improved method for finite element mesh generation of geometrically complex structures with application to the skullbase*, J. Biomech., 30 (1997), pp. 1067–1070.
- [8] J. HÄRDTLEIN AND C. PFLAUM, *Efficient and user-friendly computation of local stiffness matrices*, in Frontiers in Simulation, Simulationstechnique, 18th Symposium, Erlangen, 2005, pp. 748–753.
- [9] COMPUMEDICS NEUROSCAN, *Current Reconstruction and Imaging (CURRY), Version 4.6*, Compumedics, El Paso, TX, <http://www.neuro.com>.
- [10] M. FUCHS, R. DRENCKHAHN, H. A. WISCHMANN, AND M. WAGNER, *An improved boundary element method for realistic volume conductor modeling*, IEEE Trans. Biomed. Engrg., 45 (1998), pp. 980–997.
- [11] N. G. GENCER AND C. E. ACAR, *Sensitivity of EEG and MEG measurements to tissue conductivity*, Phys. Med. Biol., 49 (2004), pp. 701–717.
- [12] M. GNEWUCH AND S. A. SAUTER, *Boundary Integral Equations for Second Order Elliptic Boundary Value Problems*, preprint 55, MPI for Mathematics in the Sciences, Leipzig, Germany, 1999.
- [13] G. HAASE, M. KUHN, AND S. REITZINGER, *Parallel algebraic multigrid methods on distributed memory computers*, SIAM J. Sci. Comput., 24 (2002), pp. 410–427.
- [14] W. HACKBUSCH, *Elliptic Differential Equations. Theory and Numerical Treatment*, Springer-Verlag, Berlin, 1992.
- [15] H. HALLEZ, B. VANRUMSTE, P. VAN HESE, Y. D’ASSELER, I. LEMAHIEU, AND R. VAN DE WALLE, *A finite difference method with reciprocity used to incorporate anisotropy in electroencephalogram dipole source localization*, Phys. Med. Biol., 50 (2005), pp. 3787–3806.
- [16] J. HAUSEISEN, C. RAMON, H. BRAUER, AND H. NOWAK, *The influence of local conductivity changes on MEG and EEG*, Biomedizinische Technik, 45 (1999), pp. 211–214.
- [17] J. HAUSEISEN, D. S. TUCH, C. RAMON, P. H. SCHIMPF, V. J. WEDEEN, J. S. GEORGE, AND J. W. BELLIVEAU, *The influence of brain tissue anisotropy on human EEG and MEG*, NeuroImage, 15 (2002), pp. 159–166.
- [18] G. MARIN, C. GUERIN, S. BAILLET, L. GARNERO, AND G. MEUNIER, *Influence of skull anisotropy for the forward and inverse problem in EEG: Simulation studies using the FEM on realistic head models*, Human Brain Mapping, 6 (1998), pp. 250–269.
- [19] J. W. H. MELIS, O. W. WEIER, M. J. PETERS, AND A. VAN OOSTEROM, *On the numerical accuracy of the boundary element method*, IEEE Trans. Biomed. Engrg., 16 (1989), pp. 1038–1049.
- [20] M. MERTENS AND B. LÜTKENHÖNER, *Efficient neuromagnetic determination of landmarks in the somatosensory cortex*, Clinical Neurophysiol., 111 (2000), pp. 1478–1487.
- [21] M. MOHR, *Simulation of Bioelectric Fields: The Forward and Inverse Problem of Electroencephalographic Source Analysis*, Ph.D. thesis, Friedrich-Alexander-Universität Erlangen-Nürnberg, Arbeitsberichte des Instituts für Informatik, Band 37 (6), 2004.
- [22] J. C. DE MUNCK, B. W. VAN DIJK, AND H. SPEKREIJSE, *Mathematical dipoles are adequate to describe realistic generators of human brain activity*, IEEE Trans. Biomed. Engrg., 35 (1988), pp. 960–966.

- [23] J. C. DE MUNCK AND M. PETERS, *A fast method to compute the potential in the multisphere model*, IEEE Trans. Biomed. Engrg., 40 (1993), pp. 1166–1174.
- [24] S. MURAKAMI AND Y. C. OKADA, *Contributions of principal neocortical neurons to magnetoencephalography and electroencephalography signals*, J. Physiol., 575 (2006), pp. 925–936.
- [25] C. PANTEV, M. HOKE, B. LÜTKENHÖNER, AND K. LEHNERTZ, *Tonotopic organization of the auditory cortex: Pitch versus frequency representation*, Science, 246 (1989), pp. 486–488.
- [26] J. SARVAS, *Basic mathematical and electromagnetic concepts of the biomagnetic inverse problem*, Phys. Med. Biol., 32 (1987), pp. 11–22.
- [27] P. H. SCHIMPF, C. R. RAMON, AND J. HAUEISEN, *Dipole models for the EEG and MEG*, IEEE Trans. Biomed. Engrg., 49 (2002), pp. 409–418.
- [28] O. TANZER, S. JÄRVENPÄÄ, J. NENONEN, AND E. SOMERSALO, *Representation of bioelectric current sources using Whitney elements in finite element method*, Phys. Med. Biol., 50 (2005), pp. 3023–3039.
- [29] T. D. WABERSKI, H. BUCHNER, K. LEHNERTZ, A. HUFNAGEL, M. FUCHS, R. BECKMANN, AND A. RIENÄCKER, *The properties of source localization of epileptiform activity using advanced headmodelling and source reconstruction*, Brain Topography, 10 (1998), pp. 283–290.
- [30] D. WEINSTEIN, L. ZHUKOV, AND C. JOHNSON, *Lead-field bases for electroencephalography source imaging*, Annals of Biomed. Engrg., 28 (2000), pp. 1059–1066.
- [31] C. H. WOLTERS, M. KUHN, A. ANWANDER, AND S. REITZINGER, *A parallel algebraic multigrad solver for finite element method based source localization in the human brain*, Comput. Vis. Sci., 5 (2002), pp. 165–177.
- [32] C. H. WOLTERS, L. GRASEDYCK, AND W. HACKBUSCH, *Efficient computation of lead field bases and influence matrix for the FEM-based EEG and MEG inverse problem*, Inverse Problems, 20 (2004), pp. 1099–1116.
- [33] C. H. WOLTERS, A. ANWANDER, X. TRICOCHÉ, S. LEW, AND C. R. JOHNSON, *Influence of local and remote white matter conductivity anisotropy for a thalamic source on EEG/MEG field and return current computation*, Int. J. Bioelectromag., 1 (2005), pp. 203–206.
- [34] C. H. WOLTERS, A. ANWANDER, D. WEINSTEIN, M. KOCH, X. TRICOCHÉ, AND R. MACLEOD, *Influence of tissue conductivity anisotropy on EEG/MEG field and return current computation in a realistic head model: A simulation and visualization study using high-resolution finite element modeling*, NeuroImage, 30 (2006), pp. 813–826.
- [35] C. H. WOLTERS, H. KÖSTLER, C. MÖLLER, J. HÄRDTLEIN, AND A. ANWANDER, *Numerical approaches for dipole modeling in finite element method based source analysis*, in International Congress Series 1300, Elsevier Science, Amsterdam, The Netherlands, 2007, pp. 189–192.
- [36] Y. YAN, P. L. NUNEZ, AND R. T. HART, *Finite-element model of the human head: Scalp potentials due to dipole sources*, Med. Biol. Engrg. Comput., 29 (1991), pp. 475–481.